RSC Advances

PAPER

View Article Online
View Journal | View Issue

Cite this: *RSC Adv.*, 2024, **14**, 7540

Electrospun Cu–Co ferrite nanofibers: synthesis, structure, optical and magnetic properties, and anti-cancer activity†

Fatimah Alahmari, *[a] Firdos Alam Khan, [b] H. Sozeri,[c] M. Sertkol [d] and Mariusz Jaremko [e]

In this study, we investigated Cu–Co ferrite nanofibers (NFs) that were synthesized for the first time employing the electrospinning technique. The structure, phase purity and crystallite size of all the prepared NFs were revealed by powder X-ray diffraction (PXRD) analysis. The NFs crystallized in the $Fd\bar{3}m$ (no. 227) space group and the cation distribution arrangement over distinct sites in their structure was analyzed. Scanning electron microscopy (SEM) together with energy-dispersive X-ray (EDX) spectroscopy analysis showed the microstructure of the NFs and verified their expected chemical compositions. High-resolution transmission electron microscopy (TEM) images confirmed the fibrous nature and the construction of the NFs. The band gap energies derived from the UV-vis reflectance spectra showed a blue shift with an increase in the amount of Cu in the sample from 1.42 eV to 1.86 eV. Magnetization (M) as a function of magnetic field (H) measurements performed at ambient and low temperatures showed the ferrimagnetic behavior of all the NFs. The magnetic parameters including coercivity (H_c), saturation magnetization (M_s), remanent magnetization (M_r), and squareness ratio were determined from the recorded magnetization curves. At 300 K, M_s was reduced from 78.8 to 42.4 emu g^{-1}, M_r reduced from 22.8 to 7.6 emu g^{-1} and the Bohr magneton reduced from 3.3 to 1.8μ_B with an increase in the content of Cu in the samples. The same trend was observed at 10 K, where M_s was reduced from 93.7 to 50.9 emu g^{-1}, M_r reduced from 60.9 to 35.9 emu g^{-1} and the Bohr magneton reduced from 3.94 to 2.16μ_B. Alternatively, H_c has the highest values for $x = 0$ (850 Oe at 300 K and 5220 Oe at 10 K) and $x = 0.6$ (800 Oe at 300 K and 5400 Oe at 10 K). The anti-cancer activity of the NFs was evaluated using the MTT cell viability assay, showing a reduction in the viability of both HCT-116 and HeLa cancer cells compared to non-cancerous HEK-293 cells after treatment with the NFs. Apoptotic activity was examined by DAPI staining, where treatment with the NFs induced chromatin condensation and nuclear disintegration in HCT-116 cells.

Received 26th November 2023
Accepted 14th February 2024

DOI: 10.1039/d3ra08087k

rsc.li/rsc-advances

1. Introduction

Nanotechnology plays a key role in the current renaissance of our life. The super and unusual properties of materials with a nano size compared to the bulk of the same materials make them optimum choices for state-of-the-art applications.[1–3] Among the materials applied in nanotechnology, nano-sized ferrites have attracted considerable interest owing to their low cost and high efficiency in a wide range of applications including industrial, medical, and environmental applications.[1] Ferrites are inorganic materials consisting of Fe^{3+} as the main cation, coupled with O^{2-} anions and other cations such as transition, rare earth and alkaline earth metals. They are grouped according to their structures and chemical formulas into spinel, garnet, ortho and hexaferrite.[4] Spinel ferrites with the chemical formula AB_2O_4 (A is a divalent cation and B is Fe^{3+} and trivalent cations dopants if present) are the most well-known type of ferrites.[5] Among the spinel ferrites, nano-sized

[a]Department of Nanomedicine Research, Institute for Research and Medical Consultations (IRMC), Imam Abdulrahman Bin Faisal University, P. O. Box 1982, 31441 Dammam, Saudi Arabia. E-mail: fsalahmari@iau.edu.sa

[b]Department of Stem Cell Research, Institute for Research and Medical Consultations (IRMC), Imam Abdulrahman Bin Faisal University, P. O. Box 1982, 31441 Dammam, Saudi Arabia

[c]TUBITAK-UME, National Metrology Institute, P. O. Box 54, 41470 Gebze, Kocaeli, Turkey

[d]Department of Basic Science, Deanship of Preparatory Year and Supporting Studies, Imam Abdulrahman Bin Faisal University, P. O. Box 1982, Dammam, 34212, Saudi Arabia

[e]Biological and Environmental Sciences and Engineering Division, King Abdullah University of Science and Technology, Thuwal 23955-6900, Saudi Arabia

† Electronic supplementary information (ESI) available. See DOI: https://doi.org/10.1039/d3ra08087k

Co ferrites are of scientific interest due to their eco-friendly nature, strong coercivity, acceptable magnetization and high resistivity, chemical stability and mechanical hardness.[2–6] Thus, they have been used in significant applications including microwave adsorption, magnetic resonance imaging, magnetic recording, organic dye adsorption, gas sensing, catalysis and biotechnology. However, Co ferrites suffer from low electrical conductivity, low magnetostriction coefficient and huge volume expansion.[7,8]

One of the most significant features of ferrites is that their magnetic, optical, and electrical properties can be enhanced by varying their chemical composition and morphology utilizing appropriate synthesis techniques.[1,6]

For instance, doping Co ferrite nanocrystals with other transition metals such as Mn, Ni and Zn can enhance their electrical and magnetic properties and expand their applications.[9–12] In the case of nanocrystalline Cu–Co ferrite, several studies have reported the synthesis of Cu-substituted Co ferrite nanoparticles (NPs) and their modified properties with respect to unsubstituted Co ferrite. N. Velinov *et al.* synthesized Cu–Co ferrite NPs utilizing the mechanochemical method and reported their catalytic activity.[13] M. Hashim *et al.* synthesized Cu–Co ferrite NPs using the sol–gel method and studied their modified electrical properties.[14] J. Balavijayalakshmi *et al.* synthesized Cu–Co ferrite NPs *via* a coprecipitation reaction and studied the influence of varying concentrations on their dielectric properties.[15] B. Chandra Sekhar *et al.* synthesized Cu–Co ferrite *via* an auto-combustion reaction and reported the enhancement in their magnetostrictive properties and strain derivative values.[16] However, to the best of our knowledge, there is no report to date on the synthesis and characterization of Cu–Co ferrite in nanofiber form.

One-dimensional nanofibers (NFs) possess many advantages compared to other forms of nanocrystals including light weight, high surface-to-volume ratio, accessible pore structure and easy-to-modify surface. NFs can be produced in different forms including, organic, metallic and organometallic compositions. Among them, metal oxide NFs exhibit high thermal and chemical stability, making them suitable for a variety of applications. One of the most employed methods to produce nanofibers is the electrospinning technique due to its low cost, easy preparation, probability of mixing materials and mass production capability.[17]

Besides the technical importance of Co ferrites in industry, they have been used for medical applications due to their biocompatibility, activity and low toxicity.[18–20] Doping of Cu in Co ferrites is expected to enhance their bio-activity due to the role that Cu^{2+} plays in medical applications, especially in anti-cancer agents.[21–24] In this regard, the substitution of Co with Cu has been found to improve the antibacterial activity of Co ferrite nanoparticles.[25] Regarding anti-cancer activity, a Co–Cu ferrite/$Na_2Ca_2Si_3O_9$ composite (Bioglass) has been reported to have cytotoxicity against osteoblast cancer cells.[26] To the best of our knowledge, the anti-cancer activity of pure nanocrystalline Cu–Co ferrite has not been reported to date.

Herein, we introduce the use of the electrospinning technique to synthesize Cu–Co ferrite NFs for the first time. Furthermore, the structure, morphology, optical property, magnetism, and anti-cancer activity of the prepared NFs are discussed based on an increase in the content of Cu dopant in the sample.

2. Materials and methods

2.1. Instrumentation

Nanofibers (NFs) were synthesized utilizing an electrospinning system (NanoSpinner Unit INOVENSO, Standard Type, NS1, Co. Turkey). The phase purity of the obtained NFs was verified by PXRD (Rigaku Benchtop Miniflex, Tokyo, Japan X-ray powder diffractometer operating using a Cu Kα radiation generator). The NF morphology was imaged using scanning electron microscopy (SEM/TEM, FEI Titan 80–300 kV FEGS/TEM, Hillsboro, OR, USA). The presence and percentage of various merged elements were confirmed by energy dispersive X-ray spectroscopy (EDX) analysis. UV-vis diffuse reflectance spectra were measured using a JASCO V-700 spectrophotometer in the range of 200–900 nm at room temperature.

A Quantum Design SQUID-PPMS vibrating sample magnetometer (PPMS DynaCool, Quantum Design, San Diego, CA, USA) was used to measure the magnetization of the synthesized samples.

2.2. Synthesis

High-purity metal nitrates, polyvinylpyrrolidone (PVP, average $M_w \sim 1\,300\,000$) and absolute ethanol were used as received (Sigma-Aldrich). To prepare the gel solution, a stoichiometric amount of $Co(NO_3)_2 \cdot 6H_2O$, $Fe(NO_3)_3 \cdot 9H_2O$, and $Cu(NO_3)_2 \cdot 3H_2O$ was mixed with PVP in a weight ratio of about 1 : 3 before adding 10 mL ethanol and 6.6 mL H_2O and kept stirring magnetically for 2 h until the formation of a clear gel. According to the systemic study, this metal salt to PVP ratio was found to give a clear gel that was viscous enough to spin without dropping. The electrospinning synthesis was done according to our previously published procedure.[27] The obtained electrospun NF samples were left to dry in air at 100 °C for 2 h before calcination at 600 °C for 5 h.

2.3. Anti-cancer assay

2.3.1. *In vitro* cell culture. Colorectal carcinoma HCT-116 and cervical HeLa cells were selected to examine the effect of the NFs on the number and proliferation of cells. Non-cancerous HEK-293 embryonic kidney cells were used as the control group. All cell lines were purchased from ATCC (American Type Culture Collection), Manassas, Virginia, United States. The cells were cultured in 96 well culture plates with DMEM and other nutrients according to the previously described method.[28] Cell growth was performed in 96-well culture plates placed in a 5% CO_2 incubator at a temperature of 37 °C. After 24 h, when cells were 75–80% confluent, they were ready for MTT examination.

2.3.2. MTT assay. During the MTT assay, NFs (5.0 μg to 50 μg mL^{-1}) were added to HCT-116, HeLa and HEK-293 cells and kept in a CO_2 incubator. After 48 h, the cells were treated with

MTT (5 mg mL^{-1}) for 4 h in the incubator. Then, a plate reader was used to examine the plate at 570 nm. Finally, the cell viability was determined utilizing the GraphPad Prism Software 6.0 (GraphPad Software, USA).[29,30]

2.3.3. Apoptotic DAPI staining. The apoptotic nuclear structure of CHT-116 cells was studied using DAPI staining 48 h post-treatment with NFs. In the experimental group, NFs were added at 25 μg mL^{-1}, whereas in the control group, no NFs were added. Then, 48 h post-treatment, the cells were fixed in paraformaldehyde, stained with DAPI and examined by confocal microscopy (Zeiss, Germany).[31,32]

3. Results and discussion

3.1. Microstructure and morphology

The structure of $Cu_xCo_{1-x}Fe_2O_4$ ($x \leq 0.6$) NFs was studied *via* PXRD analysis. Fig. 1 displays the PXRD patterns of all the samples fitted by the Rietveld method, confirming the presence of a pure phase in each sample corresponding to the spinel ferrite structure ($Fd\bar{3}m$ space group). The as-measured PXRD patterns are presented in Fig. 1S (ESI).† The refinement of the experimental PXRD data was performed using the Rietveld method and FullProf software. Rietveld refinement is a powerful technique used to extract the crystal structure characteristics of a material from its PXRD reflections by estimating the peak intensity, position, height and width.[33] The crystallite size values were calculated using the Scherrer formula (Table 1). As shown in Table 1, the lattice constant a increased with an increase in the content of Cu^{2+} in the sample, suggesting that the dopant cation has a bigger ionic radius than the substituted one. In the present NFs, Cu^{2+} with an ionic radius of 0.70 Å substituted Fe^{3+}, which has an ionic radius of 0.67 Å ionic radius, as confirmed by the cation distribution analysis shown in Table 2. Thus, the lattice to expands with an increase in the concentration of Cu^{2+}, which is in agreement with the reported results.[10] Fig. S2† shows a plot of the relation between the lattice constant a and Cu^{2+} concentration in the sample, as represented by the x value, which shows a direct proportional relation. The crystallite size (represented by D_{XRD} in Table 1) decreases with an increase in Cu^{2+} content in the sample in response to the elongation of the lattice constant, which has the same trend as the reported Cu-substituted Co ferrite nanoparticles.[15,25,34]

Table 2 displays the cation distribution of $Cu_xCo_{1-x}Fe_2O_4$ ($0 \leq x \leq 0.6$) NFs over the tetrahedral and octahedral sites obtained from the PXRD patterns following the Bertaut method.[35,36] The XRD intensity ratios of the I_{220}/I_{440} and I_{422}/I_{400} planes were considered for the identification of the cation distribution.[36] The results show that the Fe^{3+} and Co^{2+} ions occupy both the tetrahedral sites (A-site) and octahedral sites (B-site); however, most of them are distributed over the B-site. The ratio of Co^{2+} decreases as the substitution ratio of Cu^{2+} increases. The Cu^{2+} ions only occupy the B-site at a substitution amount lower than $x = 0.6$; however, a small fraction of Cu^{2+} ions occupy the A-site for the $x = 0.6$ sample. The occupancy of the Co^{2+}, Cu^{2+} and Fe^{3+} ions depicted here is consistent with other reports.[37]

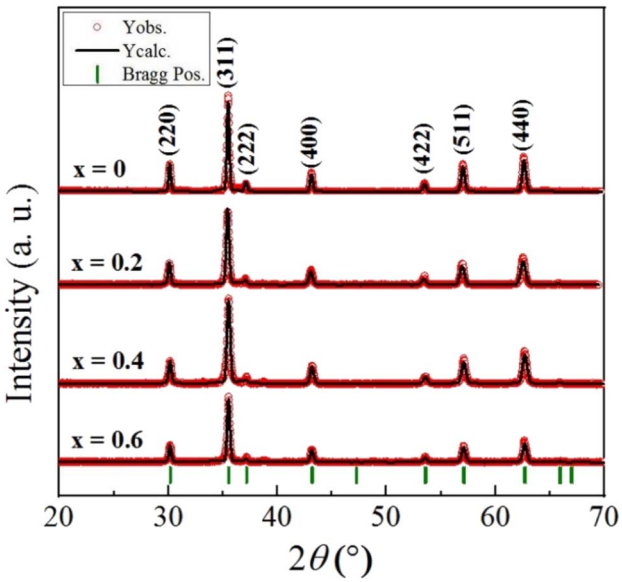

Fig. 1 PXRD patterns of $Cu_xCo_{1-x}Fe_2O_4$ ($0 \leq x \leq 0.6$) NFs fitted by the Rietveld method.

Scanning electron microscopy (SEM) and energy-dispersive X-ray spectroscopy (EDX) were used to analyze the NF samples. Fig. 2 shows the SEM/EDX images and the elemental mapping results for the lowest and highest x values of the Cu-containing samples, *i.e.*, $Cu_xCo_{1-x}Fe_2O_4$ ($x = 0.2$, 0.6). The results show that the aggregation of nanofibers containing all the involved elements with atomic ratios agrees well with the proposed chemical compositions.

Fig. 3 displays the high-resolution TEM images for $Cu_xCo_{1-x}Fe_2O_4$ ($x = 0.2$, 0.6) at different resolutions. The images captured at around 200 nm confirm the fibrous nature of the prepared material with a nano size. The images captured at 50 nm and 20 nm illustrate the multifaced grains constructing the nanofibers for both samples. The average grain size for the lowest x value sample $Cu_{0.2}Co_{0.8}Fe_2O_4$ is obviously bigger than the average size of that for the highest x value sample $Cu_{0.6}Co_{0.4}Fe_2O_4$. Thus, the grain size was reduced by increasing the amount of Cu in the sample, which agrees with the PXRD data calculation in Table 1. This result suggests that introducing Cu in the Co ferrite lattice can address one of the issues associated with Co ferrites, which is the huge volume expansion presented by their large grain size.[8] Given that the fibers are formed from the connection between the grain boundaries, a smaller grain size provides a stronger connection between the grains due to

Table 1 The structural parameter refinement calculation for $Cu_xCo_{1-x}Fe_2O_4$ ($0 \leq x \leq 0.6$) NFs with the $Fd\bar{3}m$ (no. 227) space group

x	a (Å)	V (Å)^3	D_{XRD} (nm) ±0.12	χ^2 (chi^2)	R_{Bragg}
0.0	8.381(4)	588.78	35.89	1.63	2.10
0.2	8.383(0)	589.10	31.73	1.21	1.06
0.4	8.390(8)	590.76	27.14	1.59	1.05
0.6	8.400(6)	592.83	26.31	1.72	1.23

Table 2 The cation distribution calculation for $Cu_xCo_{1-x}Fe_2O_4$ ($0 \leq x \leq 0.6$) NFs

x	Tetrahedral A-site	Octahedral B-site
0.0	$Co_{0.2}Fe_{0.8}$	$Co_{0.8}Fe_{1.2}$
0.2	$Co_{0.1}Fe_{0.9}$	$Co_{0.7}Cu_{0.2}Fe_{1.1}$
0.4	$Co_{0.05}Fe_{0.95}$	$Co_{0.55}Cu_{0.4}Fe_{1.05}$
0.6	$Cu_{0.1}Fe_{0.9}$	$Co_{0.4}Cu_{0.5}Fe_{1.1}$

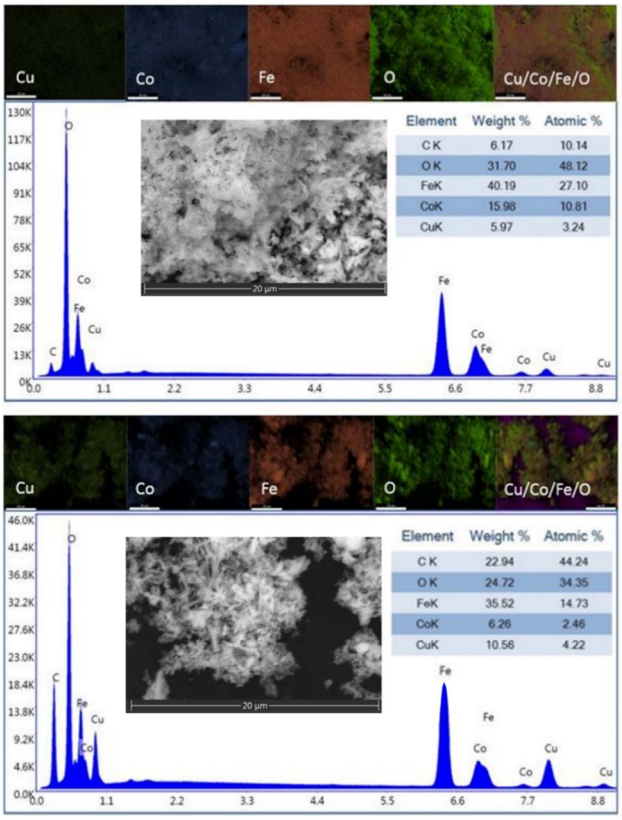

Fig. 2 SEM/EDX and elemental mapping for $Cu_xCo_{1-x}Fe_2O_4$ ($x = 0.2$ (top panel) and 0.6 (bottom panel)) NFs. In the elemental analysis graph, the X-axis represents energy (eV) and the Y-axis represents intensity (k).

the larger contact area.[38] Moreover, the thickness of the NFs is associated with the grain size. Fig. 3a shows a thinner NF for the $x = 0.2$ sample constructed by bigger grains overlapping each other, appearing as a chain-like array. Fig. 3b shows a thicker NF for the $x = 0.6$ sample constructed by multi-grain attachments along the NF due to the large contact area of the smaller grains.

3.2. UV-vis optical analysis

The optical property of the prepared NFs was studied by measuring their UV-vis diffuse reflectance spectra (Fig. S3†). The absorption data was derived from the diffuse reflectance spectra using the Kubelka–Munk function $F(R)$.[39] To determine the band gap energies (E_g) of the prepared NFs, the Tauc method was employed using the following expression:

$$(F(R)h\nu)^{1/\gamma} = B(h\nu - E_g) \quad (1)$$

where h is Planck's constant, ν is the frequency and B is a constant. The γ factor depends on the nature of the material band gap, which has a value of $\frac{1}{2}$ for a direct electron transition or 2 for an indirect electron transition.[40,41] Fig. 4 displays the Tauc plots for all the prepared NFs, which obey the direct band gap transition equation. All the prepared NFs are semiconductors with estimated band gap edges varying from 1.42 to 1.86 eV, which increase with an increase in the amount of Cu in the sample. The blue shift in the band gap throughout the samples is attributed to the decrease in crystallite size with an increase in Cu concentration from $x = 0$ to $x = 0.6$, which leads to the Brus effective mass model.[42,43] Moreover, this finding agrees well with the above-mentioned TEM results and PXRD calculation. The same behaviour has been reported for Co–Cu ferrite nanoparticles (NPs), where the band gap energies decrease with an increase in Cu concentration in the sample.[43] However, the present NF samples ($1.4 < E_g < 1.9$) have narrower band gap edges than their NP counterpart ($1.7 < E_g < 2.5$).

The characteristics of the NFs, as a conjugated material, are mainly ascribed to the superstructure of connected particles, not only the properties of individual particles. The overlap between some conduction orbitals of the conjugated particles results in a delocalization of the charge carriers along the conjugation length. Thus, the high mobility along the NF backbone results in a reduction in the bandgap energies.[44]

3.3. Magnetic analysis

The magnetic property of the $Cu_xCo_{1-x}Fe_2O_4$ ($0 \leq x \leq 0.6$) NFs was analyzed by measuring the M–H hysteresis loops in the field range of ± 7 T at a low temperature (10 K) and ambient temperature (300 K), as shown in Fig. 5. All the measured hysteresis loops show ferrimagnetic ordering behavior at both temperatures. Different magnetic parameters including saturation magnetization (M_s), coercivity (H_c), remanent magnetization (M_r) and squareness ratio were calculated using the measured curves, as listed in Table 3. The magnetization loops recorded at 300 K were saturated at high fields, whereas that recorded at 10 K were not. Therefore, the law of approach to saturation (LAS) method was used to determine the M_s values by extrapolating the linear fits of the M *vs.* $1/H^2$ plots.[45]

The saturation magnetization (M_s) values of the Cu–Co ferrite NFs decreased with an increase in the Cu content at both temperatures. The reduction in M_s for all the samples can be related to the site preference of the substituted cations in the structure of each sample, as described below.

The magnetic moments of the prepared NFs were estimated using the Néel theory in units of Bohr magneton (μ_B) according to the following equation:

$$\mu_B = \frac{M_w M_s}{5585} \quad (2)$$

where M_s is the saturation magnetization and M_w is the molecular weight of the $Cu_xCo_{1-x}Fe_2O_4$ NFs.[49] As shown in Table 3, the magnetization of the Cu–Co ferrite NFs also decreased with an increase in Cu content in the unit of μ_B.

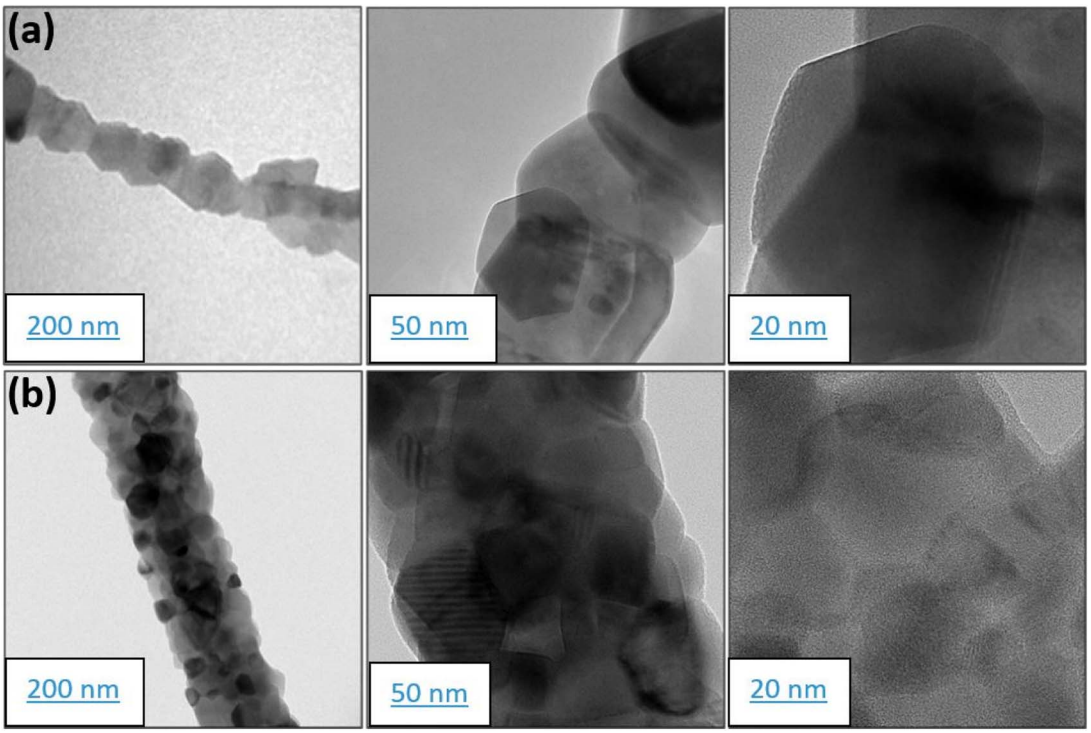

Fig. 3 High-resolution TEM images for $Cu_xCo_{1-x}Fe_2O_4$ ($x = 0.2$ (a) and 0.6 (b)) NFs.

In simple Co spinel ferrites, where the Co^{2+} ions occupy the octahedral sites and Fe^{3+} ions are distributed equally over the tetrahedral and octahedral sites, the magnetic moment is $\sim 5\mu_B$.[46–48] In this case, tuning the cation distribution in the structure affects the magnetic properties of the nanoparticles.[43] The calculated magnetic moment of the unsubstituted $CoFe_2O_4$ NFs in the present series was reduced to $\sim 3\mu_B$. Unlike simple Co ferrites, the cations distribution analysis in Table 2 reveals that in $Cu_xCo_{1-x}Fe_2O_4$ with x values from 0 to 0.4, most of the Co^{2+} ions are in the octahedral B-sites but a small amount is in the tetrahedral A-sites. When non-magnetic ions (Cu^{2+}) replace the magnetic ions (Co^{2+} and Fe^{3+}) in the octahedral site, the magnetization of the B-sublattice decreases, and thus the net magnetization, which is expressed by $M = M_B - M_A$, also decreased.[43,50] In the case of the highest Cu concentration sample ($x = 0.6$), a remarkable reduction in the magnetic moment occurred due to the site occupation rearrangement. In this case, Co^{2+} occupied only the B-sites, while a small amount of Cu^{2+} migrated to the A-sites, which is believed to be responsible for the further decrease in the magnetic moment of this sample. The magnetic ordering in spinel ferrites is subject to the superexchange mechanism between the metal ions in the octahedral and tetrahedral sites. The exchange interactions (A–A, A–B, and B–B) between the electrons of the ions in these two sublattices determine the magnetization of the ferrite structure, where the A–B interaction is the strongest one.[50,51]

The squareness ratio (SQR) is another key parameter described in the Stoner–Wohlfarth model, where a value equal or close to 0.5 means that the particles have uniaxial crystal anisotropy and they are non-interacting, resulting in a single domain structure.[52] The SQR values of the presented Cu–Co ferrite NFs are either below or above this threshold, and thus we conclude that they have a multi-domain structure, which agrees with the nature of the NFs as connected particles.

In the case of coercivity (H_c), the highest values were determined at $x = 0$ and 0.6 (Table 3). The H_c decreased with an increase in Cu content until $x = 0.4$, and then increased strongly with higher Cu concentration ($x = 0.6$). This observation can be explained based on the above-mentioned cation distribution rearrangement, which may result in a change in the Cu^{2+} spin arrangement due to its occupation of both the A and B sites in this sample only.[53] Generally, the H_c of magnetic nanoparticles is controlled by several factors such as shape anisotropy, grain size, particle distribution, morphology and magnetocrystalline anisotropy.[54,55]

The effective anisotropy constant, K_{eff}, was calculated using the M_s and H_c values for cubic anisotropy according to the following the expression:

$$H_c = 0.64\frac{K_{eff}}{M_s} \quad (3)$$

The calculated K_{eff} values are 10^4 erg g^{-1} and 10^5 erg g^{-1} orders at 300 K and 10 K, respectively.[56]

The intrinsic coercivities (H_{ci}) for all NF samples are significantly higher compared to H_c and have the same tendency with an increase in the Cu-substitution ratio (Table 3).

The magnetic parameters including M_s, H_c, and M_r extracted from the M–H loops measured at 10 K are substantially higher than the same parameters calculated from the M–H curve

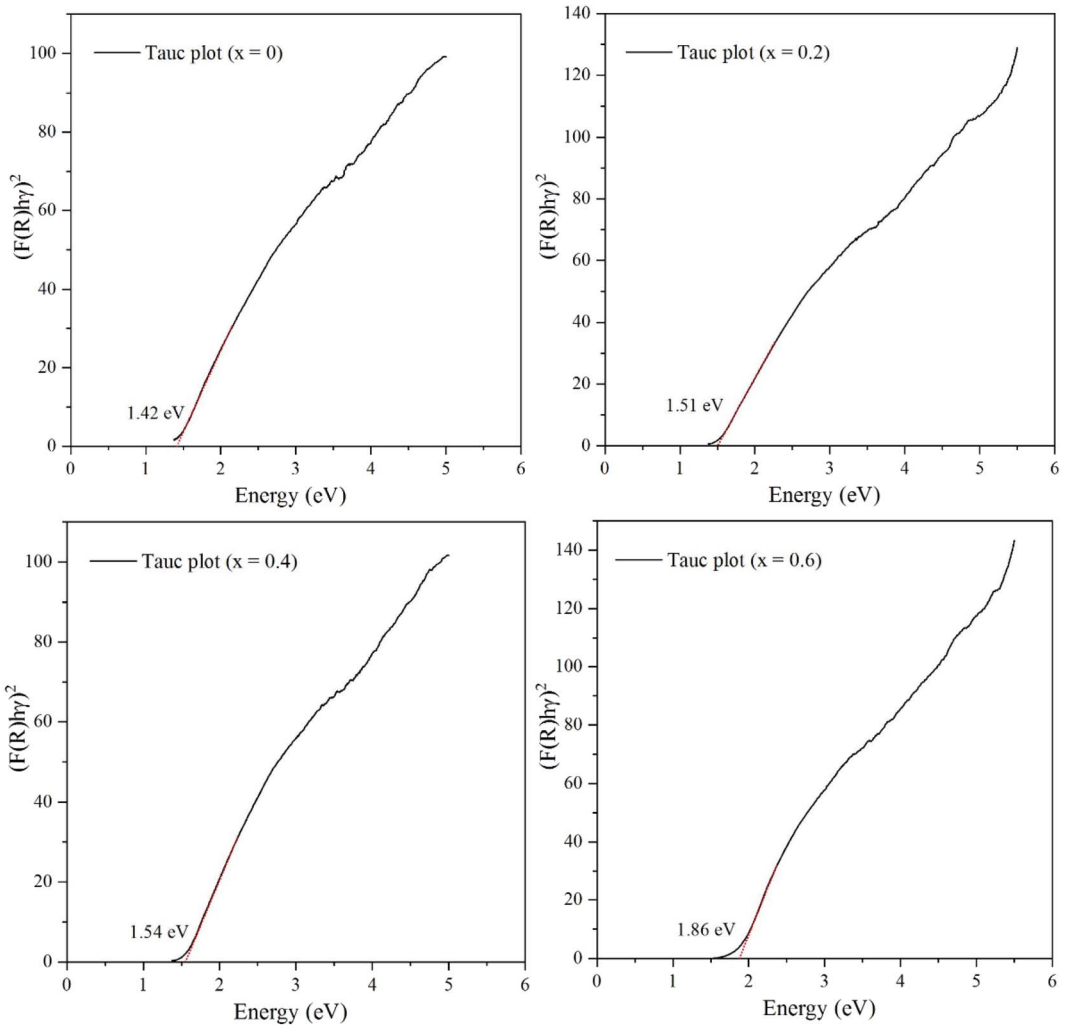

Fig. 4 Tauc plots for $Cu_xCo_{1-x}Fe_2O_4$ ($0 \leq x \leq 0.6$) NFs. The dashed red lines are the Tauc plot leaner fits to determine the band gap energies.

measured at 300 K. As the temperature decreases, the surface spin disorder and thermal fluctuation of the nanoparticles diminish, which increases the various magnetic parameters.[57]

3.4. Cell viability post treatment

The prepared NFs produced an inhibitory action on HCT-116 and HeLa cells, as revealed by the cell viability assay. The cell viability decreased in both groups after 48 h of treatment with the $Cu_xCo_{1-x}Fe_2O_4$ ($x \leq 0.6$) NFs (Fig. 6). The treated HCT-116 cells showed a significant decrease in viability, while that of the treated HeLa cells did not decrease significantly. Also, to examine whether the prepared NFs produced similar effects on normal and healthy cells, HEK-293 cells were treated with the same concentration. The viability of the HEK-293 cells decreased after the treatment, but to a lesser degree compared to HCT-116 and HeLa cells (Fig. 6).

This finding suggests that these NFs produced better cytotoxic effects on cancerous cells than the healthy cells. The inhibitory concentrations (IC_{50}) of the NFs on HCT-116 cells were 29.50 μg mL^{-1} ($x = 0$), 31.72 μg mL^{-1} ($x = 0.2$), 33.25 μg mL^{-1} ($x = 0.4$), and 36.25 μg mL^{-1} ($x = 0.6$). In the case of HeLa cells, the IC_{50} values were 29.20 μg mL^{-1} ($x = 0.0$), $x = 0.2$ (39.52 μg mL^{-1}), $x = 0.4$ (41.15 μg mL^{-1}), and $x = 0.6$ (44.50 μg mL^{-1}). This is the first study to examine the cytotoxic effects of pure nano-sized Cu–Co ferrites on human cancer cells. The cell viability and cytotoxicity of a Co–Cu ferrite/$Na_2Ca_2Si_3O_9$ (Bioglass) composite was assessed using osteoblast (MG63) cell lines for hyperthermia application.[26] Another study showed that Cu and Co MOF NPs showed anticancer activity against the SKOV3, U87MG, and LN229 cell lines.[58]

3.5. Apoptotic cancer cell death

To examine whether cancer cell death is due to apoptosis or programmed cell death, the NF samples were stained with DAPI, which is a nuclear DNA stain.[59] DAPI staining is used as a marker for apoptosis, where chromatin condensation, chromatin augmentation, and cell shrinkage are the hallmarks of apoptosis. It was found that the NF treatment induced chromatin condensation and nuclear disintegration of the colon cancer cells, as revealed by the DAPI staining (Fig. 7B–E). In

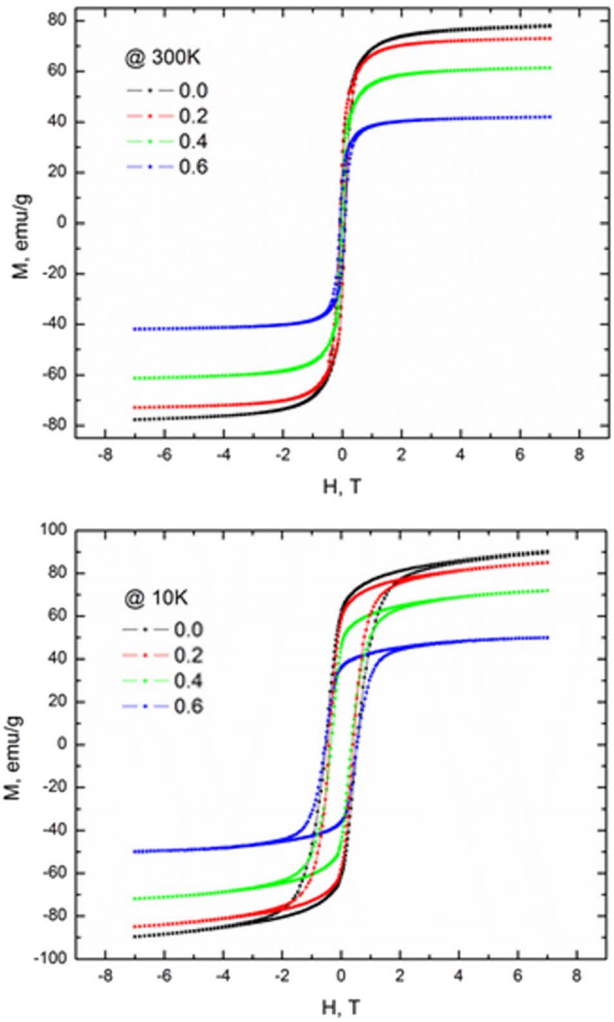

Fig. 5 M–H hysteresis loops of $Cu_xCo_{1-x}Fe_2O_4$ ($0 \leq x \leq 0.6$) NFs at 10 K and 300 K.

contrast, when colon cancer cells were not treated with NFs, no inhibitory action was observed in the cancer cells (Fig. 7A). A decrease in cancer cells may occur due to programmed cell death resulting from oxidative stress (apoptosis) as a reaction to nano-sized Co ferrites.[19,27] Moreover, the inhibitory action of the present NFs on cancer cells was found to increase with an increase in Cu concentration in the sample. The role of Cu is critical in cancer treatment, where in the case of nanomaterials containing Cu, several studies have examined their inhibitory action against cancer cells. Copper oxide nanowires decorated with folic acid (CuO-Nw–FA) showed enhanced cellular uptake in triple negative breast cancer (TNBC) cells.[60] $CuFe_2O_4$ hybrid nanoradiosensitizers ($CuFe_2O_4$@BSA–FA–CUR) produced a cytotoxic effect on tumor cells through an *in vitro* study, and also showed high cancer suppression efficiency an *in vivo* experiment, where $CuFe_2O_4$@BSA–FA–CUR nanoplatforms led to complete tumor ablation in almost all the treated mice.[61] The cytotoxicity of a CuO NP and chitosan composite was examined against human breast cancer MDA-MB-231 and lung cancer A549 cell lines.[62] The combination of disulfiram and Cu nanoparticles showed significant anti-cancer activity in CT26 colorectal cancer cells in both *in vitro* and *in vivo* studies, where significant apoptosis was induced, which caused the elimination of tumors in animals.[63] In addition, Cu nanoparticles showed a cytotoxic effect on the SW480 human colorectal cancer cell line.[64] Thus, the prepared NFs, which contain Co and Cu, were expected to have anti-cancer activity.

4. Conclusion

The electrospinning synthesis of $Cu_xCo_{1-x}Fe_2O_4$ ($0 \leq x \leq 0.6$) NFs was successfully achieved. The structure information, phase purity, grain size and cation distribution for all prepared NFs were estimated from the PXRD data. The microstructure and chemical composition of the NF samples were investigated using SEM/EDX analysis. The high-resolution TEM images illustrated the nanofiber nature of the studied samples and the agglomeration of the grains within the NFs. The prepared NFs are semiconductors, with their band gap edges narrowing with an increase in Cu content in the sample. The possibility for the optical property engineering of these NFs makes them potential candidates for photocatalysis applications. Furthermore, the magnetic properties such as M_s, H_c and H_{ci} of these samples were determined by M–H magnetization measurements at low and room temperature. The tendency of these parameters to

Table 3 Magnetic parameters of $Cu_xCo_{1-x}Fe_2O_4$ ($0 \leq x \leq 0.6$) NFs at 10 K and 300 K

x	M_s (emu g^{-1})	M_r (emu g^{-1})	H_c (Oe)	SQR	Bohr magneton, μ_B	K_{eff} (erg g^{-1})	H_{ci} (Oe)
@300 K							
0.0	78.8	22.8	850	0.29	3.31	10.5×10^4	2656
0.2	73.5	22.8	741	0.31	3.10	8.51×10^4	2316
0.4	62.0	13.6	297	0.22	2.63	2.88×10^4	928
0.6	42.4	7.6	800	0.18	1.80	5.30×10^4	2500
@10 K							
0.0	93.7	60.9	5220	0.65	3.94	7.64×10^5	16 313
0.2	88.3	58.2	4160	0.66	3.72	5.74×10^5	13 000
0.4	74.8	45.1	3420	0.60	3.17	4.00×10^5	10 688
0.6	50.9	35.9	5400	0.71	2.16	4.29×10^5	16 875

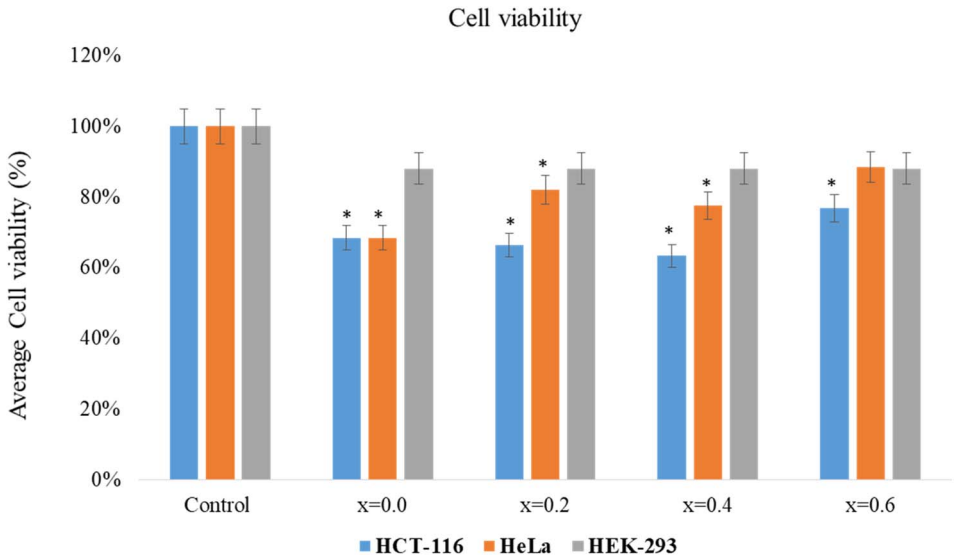

Fig. 6 MTT assay showing the effect of 25 μg per mL $Cu_xCo_{1-x}Fe_2O_4$ ($x \leq 0.60$) NFs on HCT-116 cells, HeLa cells and HEK-293 cells after 48 h of treatment. *$p < 0.05$.

increase or decrease was explained based on the increase in the concentration of Cu^{2+} throughout the samples and the cation distribution over the A and B sites. At 10 K, both the M_s and H_c values for each sample are higher than that of the same sample at ambient temperature due to the weakening of the thermal fluctuations of magnetic moments.

The bioactivity of the prepared NFs was examined using a cell viability assay, which showed a substantial decline in the cell viability of cancerous cells (HCT-116) compared to normal cells (HEK-293) after treatment with NFs. Although the cancerous cells (HeLa) treated with NFs showed less inhibition action compared to the latter, it was still higher than that in the normal cells (HEK-293). Apoptotic activity was examined by DAPI staining after treatment with NFs, which caused chromatin condensation and nuclear disintegration in colon cancer cells. The results showed that an increase in the Cu dopant ratio enhanced the bioactivity of the Co ferrites, making them a potential candidate for biomedical applications.

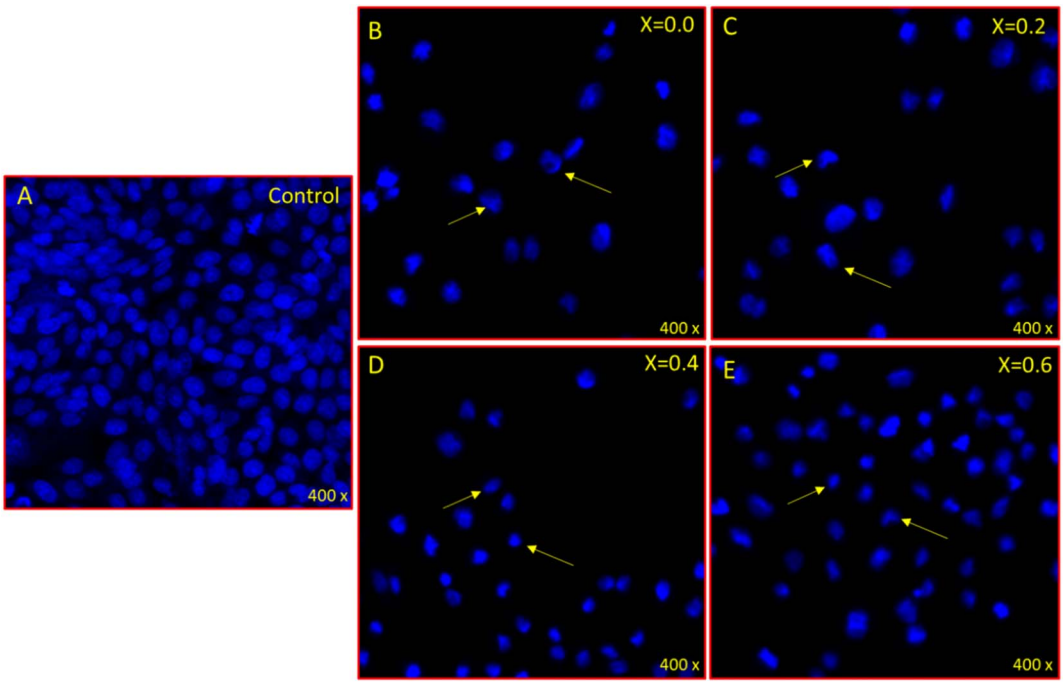

Fig. 7 (A–E) Impact of NFs on HeLa cells stained with DAPI, 48 h post-treatment. (A) (Control), (B) ($x = 0.0$), (C) ($x = 0.2$), (D) ($x = 0.4$), and (E) ($x = 0.6$). NF dose was 25 μg mL^{-1}. Arrows show nuclear condensation, fragmentation, and cell membrane disruption.

Conflicts of interest

There are no conflicts to declare.

Acknowledgements

The study was supported by the Deanship of Scientific Research, Imam Abdulrahman Bin Faisal University, Dammam, Saudi Arabia, and project number IRMC-015-2019.

References

1 S. Hazra and N. Ghosh, Preparation of nanoferrites and their applications, *J. Nanosci. Nanotechnol.*, 2014, **14**(2), 1983–2000.

2 Y. Zhang, Z. Yang, D. Yin, Y. Liu, C. Fei, R. Xiong, J. Shi and G. Yan, Composition and magnetic properties of cobalt ferrite nano-particles prepared by the co-precipitation method, *Magn. Magn. Mater.*, 2010, **322**(21), 3470–3475.

3 T. Dippong, E. A. Levei and O. Cadar, Recent advances in synthesis and applications of MFe_2O_4 (M= Co, Cu, Mn, Ni, Zn) nanoparticles, *Nanomaterials*, 2021, **11**(6), 1560.

4 A. Goldman, Crystal Structure of Ferrites, *Modern Ferrite Technology*, Springer, 2006.

5 G. Pilania, V. Kocevski, J. A. Valdez, C. R. Kreller and B. P. Uberuaga, Prediction of structure and cation ordering in an ordered normal-inverse double spinel, *Commun. Mater.*, 2020, **1**(1), 84.

6 S. Jauhar, J. Kaur, A. Goyal and S. Singhal, Tuning the properties of cobalt ferrite: a road towards diverse applications, *RSC Adv.*, 2016, **6**(100), 97694–97719.

7 M. Sajjia, A. Baroutaji and A. G. Olabi, The introduction of cobalt ferrite nanoparticles as a solution for magnetostrictive applications, *Reference Module in Materials Science and Materials Engineering*, Elsevier, 2022.

8 H. M. K. Tedjieukeng, P. K. Tsobnang, R. L. Fomekong, E. P. Etape, P. A. Joy, A. Delcorte and J. N. Lambi, Structural characterization and magnetic properties of undoped and copper-doped cobalt ferrite nanoparticles prepared by the octanoate coprecipitation route at very low dopant concentrations, *RSC Adv.*, 2018, **8**(67), 38621–38630.

9 A. Kumar, P. Sharma and D. Varshney, Structural, vibrational and dielectric study of Ni doped spinel Co ferrites: $Co_{1-x}Ni_xFe_2O_4$ (x=0.0, 0.5, 1.0), *Ceram. Int.*, 2014, **40**(8, part B), 12855–12860.

10 N. Somaiah, T. V. Jayaraman, P. A. Joy and D. Das, Magnetic and magnetoelastic properties of Zn-doped cobalt-ferrites—$CoFe_{2-x}Zn_xO_4$ (x=0, 0.1, 0.2, and 0.3), *J. Magn. Magn. Mater.*, 2012, **324**(14), 2286–2291.

11 A. Omelyanchik, G. Singh, M. Volochaev, A. Sokolov, V. Rodionova and D. Peddis, Tunable magnetic properties of Ni-doped $CoFe_2O_4$ nanoparticles prepared by the sol–gel citrate self-combustion method, *J. Magn. Magn. Mater.*, 2019, **476**, 387–391.

12 C. H. Kim, Y. Myung, Y. J. Cho, H. S. Kim, S.-H. Park, J. Park, J.-Y. Kim and B. Kim, Electronic Structure of Vertically Aligned Mn-Doped $CoFe_2O_4$ Nanowires and Their Application as Humidity Sensors and Photodetectors, *J. Phys. Chem. C*, 2009, **113**(17), 7085–7090.

13 N. Velinov, D. Dimitrov, K. Koleva, K. Ivanov and I. Mitov, Mechanochemical Synthesis and Characterization of Nanocrystalline Copper–Cobalt Ferrites, *Acta Metall. Sin. (Engl. Lett.)*, 2015, **28**(3), 367–372.

14 M. Hashim, S. Kumar, B. H. Koo, S. E. Shirsath, E. M. Mohammed, J. Shah, R. K. Kotnala, H. K. Choi, H. Chung and R. Kumar, Structural, electrical and magnetic properties of Co–Cu ferrite nanoparticles, *J. Alloys Compd.*, 2012, **518**, 11–18.

15 J. Balavijayalakshmi, N. Suriyanarayanan, R. Jayaprakash and V. Gopalakrishnan, Effect of Concentration on Dielectric Properties of Co-Cu Ferrite Nano Particles, *Phys. Procedia*, 2013, **49**, 49–57.

16 B. Chandra Sekhar, G. S. N. Rao, O. F. Caltun, B. Dhana Lakshmi, B. Parvatheeswara Rao and P. S. V. Subba Rao, Magnetic and magnetostrictive properties of Cu substituted Co-ferrites, *J. Magn. Magn. Mater.*, 2016, **398**, 59–63.

17 (*a*) J. Xue, T. Wu, Y. Dai and Y. Xia, Electrospinning and Electrospun Nanofibers: Methods, Materials, and Applications, *Chem. Rev.*, 2019, **119**(8), 5298–5415; (*b*) S. Zhang, W. Zuo, P. Wu, X. Meng, C. Sun, D. Zhang, J. Dai and Y. Ju, Dual signal output ratiometric biosensor platform with regulable nanofiber-mediated signal amplification strategy for ultrasensitive detection of tumor biomarker, *Chem. Eng. J.*, 2023, **469**, 144026; (*c*) X. Zhang, Y. Meng, B. Gong, T. Wang, Y. Lu, L. Zhang and J. Xue, Electrospun nanofibers for manipulating soft tissue regeneration, *J. Mater. Chem. B*, 2022, **10**(37), 7281–7308.

18 S. Amiri and H. Shokrollahi, The role of cobalt ferrite magnetic nanoparticles in medical science, *Mater. Sci. Eng., C*, 2013, **33**(1), 1–8.

19 S. Y. Srinivasan, K. M. Paknikar, D. Bodas and V. Gajbhiye, Applications of cobalt ferrite nanoparticles in biomedical nanotechnology, *Nanomedicine*, 2018, **13**(10), 1221–1238.

20 E. Fantechi, C. Innocenti, M. Zanardelli, M. Fittipaldi, E. Falvo, M. Carbo, V. Shullani, L. d. C. Mannelli, C. Ghelardini, A. M. Ferretti, A. Ponti, C. Sangregorio and P. Ceci, A Smart Platform for Hyperthermia Application in Cancer Treatment: Cobalt-Doped Ferrite Nanoparticles Mineralized in Human Ferritin Cages, *ACS Nano*, 2014, **8**(5), 4705–4719.

21 C. Santini, M. Pellei, V. Gandin, M. Porchia, F. Tisato and C. Marzano, Advances in Copper Complexes as Anticancer Agents, *Chem. Rev.*, 2014, **114**(1), 815–862.

22 J. Kurian, B. B. Lahiri, M. J. Mathew and J. Philip, High magnetic fluid hyperthermia efficiency in copper ferrite nanoparticles prepared by solvothermal and hydrothermal methods, *J. Magn. Magn. Mater.*, 2021, **538**, 168233.

23 A.-R. Phull, A. Ali, K. R. Dhong, M. Zia, P. G. Mahajan and H.-J. Park, Synthesis, characterization, anticancer activity assessment and apoptosis signaling of fucoidan mediated copper oxide nanoparticles, *Arab. J. Chem.*, 2021, **14**(8), 103250.

24 A. Samavati, M. K. Mustafa, A. F. Ismail, M. H. D. Othman and M. Rahman, Copper-substituted cobalt ferrite nanoparticles: structural, optical and antibacterial properties, *Mater. Express*, 2016, **6**(6), 473–482.

25 A. Samavati and A. F. Ismail, Antibacterial properties of copper-substituted cobalt ferrite nanoparticles synthesized by co-precipitation method, *Particuology*, 2017, **30**, 158–163.

26 K. A. Sampath, T. Himanshu, B. Kevin and S. P. Singh, Structural, magnetic and *in vitro* bioactivity of co-cu ferrite and bioglass composite for hyperthermia in bone tissue engineering, *Bioceram. Dev. Appl.*, 2016, **6**, DOI: 10.4172/2090-5025.100091.

27 F. Alahmari, S. Rehman, M. Almessiere, F. A. Khan, Y. Slimani and A. Baykal, Synthesis of $Ni_{0.5}Co_{0.5-x}CdxFe_{1.7}8Nd_{0.02}O_4$ ($x \leq 0.25$) nanofibers by using electrospinning technique induce anti-cancer and anti-bacterial activities, *J. Biomol. Struct. Dyn.*, 2021, **39**(9), 3186–3193.

28 S. Rehman, M. A. Almessiere, F. A. Khan, A. D. Korkmaz, N. Tashkandi, Y. Slimani and A. Baykal, Synthesis and biological characterization of $Mn_{0.5}Zn_{0.5}Eu_xDy_xFe_{1.8-2x}O_4$ nanoparticles by sonochemical approach, *Mater. Sci. Eng., C*, 2020, **109**, 110534.

29 S. S. Al-Jameel, M. A. Almessiere, F. A. Khan, N. Taskhandi, Y. Slimani, N. S. Al-Saleh, A. Manikandan, E. A. Al-Suhaimi and A. Baykal, Synthesis, Characterization, Anti-Cancer Analysis of $Sr_{0.5}Ba_{0.5}Dy_xSm_xFe_{8-2x}O_{19}$ ($0.00 \leq x \leq 1.0$) Microsphere Nanocomposites, *Nanomaterials*, 2021, **11**(3), 700.

30 M. A. Almessiere, Y. Slimani, S. Rehman, F. A. Khan, E. G. Polat, A. Sadaqat, S. E. Shirsath and A. Baykal, Synthesis of Dy-Y co-substituted manganese-zinc spinel nanoferrites induced anti-bacterial and anti-cancer activities: Comparison between sonochemical and sol-gel auto-combustion methods, *Mater. Sci. Eng., C*, 2020, **116**, 111186.

31 S. Rehman, R. Farooq, R. Jermy, S. M. Asiri, V. Ravinayagam, R. Al Jindan, Z. Alsalem, M. A. Shah, Z. Reshi, H. Sabit and F. A. Khan, A Wild Fomes fomentarius for Biomediation of One Pot Synthesis of Titanium Oxide and Silver Nanoparticles for Antibacterial and Anticancer Application, *Biomolecules*, 2020, **10**(4), 622.

32 S. Rehman, S. M. Asiri, F. A. Khan, B. R. Jermy, H. Khan, S. Akhtar, R. A. Jindan, K. M. Khan and A. Qurashi, Biocompatible Tin Oxide Nanoparticles: Synthesis, Antibacterial, Anticandidal and Cytotoxic Activities, *ChemistrySelect*, 2019, **4**(14), 4013–4017.

33 H. M. Rietveld, A profile refinement method for nuclear and magnetic structures, *J. Appl. Crystallogr.*, 1969, **2**(2), 65–71.

34 A. Bishnoi, S. Kumar and N. Joshi, Wide-angle X-ray diffraction (WXRD): technique for characterization of nanomaterials and polymer nanocomposites, in *Microscopy Methods in Nanomaterials Characterization*, Elsevier, 2017.

35 S. E. Shirsath, M. L. Mane, Y. Yasukawa, X. Liu and A. Morisako, Chemical tuning of structure formation and combustion process in $CoDy_{0.1}Fe_{1.9}O_4$ nanoparticles: influence@pH, *J. Nanopart. Res.*, 2013, **15**(10), 1976.

36 S. E. Shirsath, M. L. Mane, Y. Yasukawa, X. Liu and A. Morisako, Self-ignited high temperature synthesis and enhanced super-exchange interactions of Ho^{3+}–Mn^{2+}–Fe^{3+}–O^{2-} ferromagnetic nanoparticles, *Phys. Chem. Chem. Phys.*, 2014, **16**(6), 2347–2357.

37 *Handbook of Sol-Gel Science and Technology: Processing, Characterization and Applications*, ed. L. Klein, M. Aparicio and A. Jitianu, Springer, 2018.

38 V. V. Rodaev, A. I. Tyurin, S. S. Razlivalova, V. V. Korenkov and Y. I. Golovin, Effect of Zirconia Nanofibers Structure Evolution on the Hardness and Young's Modulus of Their Mats, *Polymers*, 2021, **13**(22), 3932.

39 G. Kortüm, W. Braun and G. Herzog, Principles and techniques of diffuse-reflectance spectroscopy, *Angew. Chem., Int. Ed. Engl.*, 1963, **2**(7), 333–341.

40 J. Tauc, R. Grigorovici and A. Vancu, Optical Properties And Electronic Structure of Amorphous Germanium, *Phys. Status Solidi B*, 1966, **15**(2), 627–637.

41 P. Makuła, M. Pacia and W. Macyk, How to correctly determine the band gap energy of modified semiconductor photocatalysts based on UV–Vis spectra, *J. Phys. Chem. Lett.*, 2018, **9**(23), 6814–6817.

42 H. Lin, C. P. Huang, W. Li, C. Ni, S. I. Shah and Y. H. Tseng, Size dependency of nanocrystalline TiO_2 on its optical property and photocatalytic reactivity exemplified by 2-chlorophenol, *Appl. Catal., B*, 2006, **68**(1–2), 1–11.

43 T. Zeeshan, S. Anjum, H. Iqbal and R. Zia, Substitutional effect of copper on the cation distribution in cobalt chromium ferrites and their structural and magnetic properties, *Mater. Sci.-Pol.*, 2018, **36**(2), 255–263.

44 T. R. Shojaei, A. Hajalilou, M. Tabatabaei, H. Mobli and M. Aghbashlo, Characterization and evaluation of nanofiber materials, *Handbook of Nanofibers*, Springer, 2019.

45 L. Néel, R. Pauthenet, G. Rimet and V. S. Giron, On the laws of magnetization of ferromagnetic single crystals and polycrystals. Application to uniaxial compounds, *J. Appl. Phys.*, 1960, **31**(5), S27–S29.

46 S. Joshi and M. Kumar, Effect of Ni^{2+} substitution on structural, magnetic, dielectric and optical properties of mixed spinel $CoFe_2O_4$ nanoparticles, *Ceram. Int.*, 2016, **42**(16), 18154–18165.

47 S. Sharmin, E. Kita, M. Kishimoto, H. Latiff and H. Yanagihara, Effect of Synthesis Method on Particle Size and Magnetic and Structural Properties of Co–Ni Ferrites, *IEEE Trans. Magn.*, 2018, **54**(11), 1–4.

48 N. Adeela, K. Maaz, U. Khan, S. Karim, A. Nisar, M. Ahmad, G. Ali, X. Han, J. Duan and J. Liu, Influence of manganese substitution on structural and magnetic properties of $CoFe_2O_4$ nanoparticles, *J. Alloys Compd.*, 2015, **639**, 533–540.

49 J. S. Smart, The Néel theory of ferrimagnetism, *Am. J. Phys.*, 1955, **23**(6), 356–370.

50 X. Zeng, J. Zhang, S. Zhu, X. Deng, H. Ma, J. Zhang, Q. Zhang, P. Li, D. Xue and N. J. Mellors, Direct observation of cation distributions of ideal inverse spinel $CoFe_2O_4$ nanofibres and correlated magnetic properties, *Nanoscale*, 2017, **9**(22), 7493–7500.

51 F. Alahmari, M. A. Almessiere, Y. Slimani, H. Güngüneş, S. E. Shirsath, S. Akhtar, M. Jaremko and A. Baykal, Synthesis and characterization of electrospun $Ni_{0.5}Co_{0.5-x}Cd_xNd_{0.02}Fe_{1.78}O_4$ nanofibers, *Nano-Struct. Nano-Objects*, 2020, **24**, 100542.

52 E. C. Stoner and E. Wohlfarth, A mechanism of magnetic hysteresis in heterogeneous alloys, *Philos. Trans. R. Soc. London, Ser. A*, 1948, **240**(826), 599–642.

53 M. S. Seehra and A. Punnoose, Particle Size Dependence of Exchange-Bias and Coercivity in CuO Nanoparticles, *Solid State Commun.*, 2003, **128**, 299–302.

54 S. More, R. Kadam, A. Kadam, D. Mane and G. Bichile, Structural properties and magnetic interactions in Al^{3+} and Cr^{3+} co-substituted $CoFe_2O_4$ ferrite, *Open Chem.*, 2010, **8**(2), 419–425.

55 M. Almessiere, Y. Slimani, H. El Sayed and A. Baykal, Morphology and magnetic traits of strontium nanohexaferrites: effects of manganese/yttrium co-substitution, *J. Rare Earths*, 2019, **37**(7), 732–740.

56 K. Praveena and K. Sadhana, Ferromagnetic properties of Zn substituted spinel ferrites for high frequency applications, *Int. J. Sci. Res.*, 2015, **5**(4), 1–21.

57 A. G. Kolhatkar, A. C. Jamison, D. Litvinov, R. C. Willson and T. R. Lee, Tuning the magnetic properties of nanoparticles, *Int. J. Mol. Sci.*, 2013, **14**(8), 15977–16009.

58 I. Han, S. A. Choi and D. N. Lee, Therapeutic Application of Metal-Organic Frameworks Composed of Copper, Cobalt, and Zinc: Their Anticancer Activity and Mechanism, *Pharmaceutics*, 2022, **14**(2), 378.

59 T. M. Alfareed, Y. Slimani, M. A. Almessiere, M. Nawaz, F. A. Khan, A. Baykal and E. A. Al-Suhaimi, Biocompatibility and colorectal anti-cancer activity study of nanosized $BaTiO_3$ coated spinel ferrites, *Sci. Rep.*, 2022, **12**(1), 14127.

60 M. Ahir, S. Bhattacharya, S. Karmakar, A. Mukhopadhyay, S. Mukherjee, S. Ghosh, S. Chattopadhyay, P. Patra and A. Adhikary, Tailored-CuO-nanowire decorated with folic acid mediated coupling of the mitochondrial-ROS generation and miR425-PTEN axis in furnishing potent anti-cancer activity in human triple negative breast carcinoma cells, *Biomaterials*, 2016, **76**, 115–132.

61 M. Salehiabar, M. Ghaffarlou, A. Mohammadi, N. Mousazadeh, H. Rahimi, F. Abhari, H. Rashidzadeh, L. Nasehi, H. Rezaeejam, M. Barsbay and Y. N. Ertas, Targeted $CuFe_2O_4$ hybrid nanoradiosensitizers for synchronous chemoradiotherapy, *J. Controlled Release*, 2023, **353**, 850–863.

62 S. Sathiyavimal, S. Vasantharaj, T. Kaliannan, H. A. Garalleh, M. Garaleh, K. Brindhadevi, N. T. L. Chi, A. Sharma and A. Pugazhendhi, Bio-functionalized copper oxide/chitosan nanocomposite using Sida cordifolia and their efficient properties of antibacterial, anticancer activity against on breast and lung cancer cell lines, *Environ. Res.*, 2022, 114986.

63 Z. Jiapaer, L. Zhang, W. Ma, H. Liu, C. Li, W. Huang and S. Shao, Disulfiram-loaded hollow copper sulfide nanoparticles show anti-tumor effects in preclinical models of colorectal cancer, *Biochem. Biophys. Res. Commun.*, 2022, **635**, 291–298.

64 P. Ghasemi, G. Shafiee, N. Ziamajidi and R. Abbasalipourkabir, Copper Nanoparticles Induce Apoptosis and Oxidative Stress in SW480 Human Colon Cancer Cell Line, *Biol. Trace Elem. Res.*, 2022, 1–9.